Structural and electrolyte properties of Li$_4$P$_2$S$_6$

Zachary D. Hood [a,1], Cameron Kates [b,2], Melanie Kirkham [c], Shiba Adhikari [d], Chengdu Liang [a,3], N.A.W. Holzwarth [b,*]

[a] Center for Nanophase Materials Sciences, Oak Ridge National Laboratory, Oak Ridge, TN 37831, USA
[b] Department of Physics, Wake Forest University, Winston-Salem, NC 27109-7507, USA
[c] Spallation Neutron Source, Oak Ridge National Laboratory, Oak Ridge, TN 37831, USA
[d] Department of Chemistry, Wake Forest University, Winston-Salem, NC 27109-7486, USA

ARTICLE INFO

ABSTRACT

Experiment and simulations are used to investigate the structural and electrolyte properties of Li$_4$P$_2$S$_6$. Compared with other thiophosphate materials, Li$_4$P$_2$S$_6$ is quite stable, maintaining its crystal structure up to temperatures as high as 950 °C in vacuum and up to 280 °C in air. While its ionic conductivity is small, 2.38×10^{-7} S/cm at 25 °C and 2.33×10^{-6} S/cm at 100 °C, its Arrhenius activation energy of 0.29 eV is similar to technologically viable electrolytes. Computer simulations provide insight into the causes and effects of disorder in this material and also indicate that the mechanism of the ion conduction is dominated by interstitial sites.

1. Introduction

Recently, there has been renewed interest in the development of all-solid state batteries [1–3], following the discovery of highly conducting solid electrolytes such as Li$_{10}$GeP$_2$S$_{12}$ [4] and nano-porous β-Li$_3$PS$_4$ [5]. Development of the all solid state battery technology motivates continued research on solid electrolytes focusing both on the continued improvement of ionic conductivity and on increasing the structural and chemical stability.

As an example of a relatively stable solid electrolyte, Li$_4$P$_2$S$_6$ has been identified in several high temperature preparations of lithium thiophosphate electrolytes as a synthesis or decomposition product [6–8]. Its characteristic P–P bond may be partly responsible for its relative stability. Early structural analysis [9] found the P sites to be disordered. Our previous simulations [10] found a related low energy structure with ordered P sites. We report here a re-examination of the simulation results and new measurements which reveal interesting details of the structure and electrolyte properties of Li$_4$P$_2$S$_6$.

Section 2 details the experimental and simulation methods used in this study. Section 3.1 presents results on the synthesis and sample morphology. Structural properties are presented in Section 3.2 including a consideration of the effects of the disordered placement of the P$_2$S$_6$ building blocks. Results concerning the stability of Li$_4$P$_2$S$_6$ are presented in Section 3.3. Electrochemical results and simulations are presented in Section 3.4. A summary and conclusions are given in Section 4.

2. Methods

2.1. Experimental procedures

2.1.1. Synthesis of Li$_4$P$_2$S$_6$

The synthesis of Li$_4$P$_2$S$_6$ was based on high temperature solid state reaction methods similar to procedures found in the literature [9,11]. Reagent-grade Li$_2$S (Alfa Aesar, 99.9%) and P$_2$S$_5$ (Sigma-Aldrich, 99%) crystalline powders were ground with a mortar and pestle for 20 min and sealed in an evacuated quartz tube to form lithium thiophosphate using the following reaction:

$$2Li_2S + P_2S_5 \rightarrow Li_4P_2S_6 + S. \tag{1}$$

Since the starting materials are hygroscopic and sensitive to air, this preparation was performed in an Ar-filled glove box.

Because we have found that the same phase of Li$_4$P$_2$S$_6$ can be formed at temperatures as low as 750 °C and at temperatures as high as 900 °C, two synthetic routes were explored. For the higher temperature synthesis, the prepared powder was heated to 900 °C for 20 h and held at 450 °C for 24 h in an electric furnace with a ramp up/down of 100 °C/h.

* Corresponding author.
E-mail address: natalie@wfu.edu (N.A.W. Holzwarth).
[1] Current affiliation: School of Chemistry and Biochemistry, Georgia Institute of Technology, USA.
[2] Current affiliation: Pratt School of Engineering, Duke University, USA.
[3] Current affiliation: Research Institute of Ningde Amperex Technology Limited, China.

The reaction product contained elemental sulfur which was removed by stirring the powder in anhydrous acetronitrile for 1 h. The powder was then filtered, and dried at 150 °C under vacuum for 2 h, producing a phase-pure material, as evidenced by X-ray diffraction data. For the lower temperature synthesis, $Li_4P_2S_6$ was heated to 750 °C for 48 h with a ramp up/down at a rate of 100 °C/h, and after similar processing in anhydrous acetronitrile, the reaction yields the same phase-pure product. Both synthetic routes yielded $Li_4P_2S_6$ with the same electrolyte properties.

2.1.2. Temperature dependent structural characterization

A PANalytical X'Pert Pro Powder Diffractometer with copper K_α radiation was used to complete all of the X-ray diffraction (XRD) analysis. Samples were placed on quartz slides for XRD analysis. Low temperature XRD measurements were completed using the Oxford Systems PheniX Cryostat over the range $15 \leq T \leq 298$ K. The software package HighScore Plus was used to complete Rietveld refinement and structural analysis. Scanning electron microscopy (SEM) images were collected using a Bruker Merlin SEM.

In addition, time-of-flight neutron diffraction results were collected at Oak Ridge National Laboratory using the POWGEN powder diffractometer at the Spallation Neutron Source. Samples were prepared with 700 mg of $Li_4P_2S_6$ loaded into a vanadium can (diameter 6 mm), sealed with an aluminum lid and copper gasket, and fitted with a titanium collar. The time-of-flight neutron diffraction patterns were collected at 300 K and 15 K over the range of diffraction plane d spacings of 0.4–9.0 Å. The time-of-flight neutron refinements were completed using the GSAS and EXPGUI software packages [12].

The thermal response of $Li_4P_2S_6$ was measured by using a TA Q600 differential scanning calorimeter fitted with a platinum/platinum–rhodium thermocouple. Measurements were taken on a 4.0 mg sample of $Li_4P_2S_6$ placed into a ceramic cup and heated to 970 °C at a rate of 10 °C/min under conditions of either constant flow of air or constant flow of argon gas. The percent weight loss was calculated from the initial weight of the sample.

2.1.3. Electrochemical characterization

In order to prepare the sample for electrochemical measurements, further processing was undertaken in the glove box. First, ball milling with Y-ZrO₂ beads having a mixture of 3 and 5 mm diameter using a ratio of 1:25 ($Li_4P_2S_4$:ball milling media) in an 8000M Spex MixerMill was used to reduce the $Li_4P_2S_6$ particle size. Then, the powder was cold-pressed at 300 MPa to form a pellet. XRD data confirmed that the ball milling media did not react with $Li_4P_2S_6$.

Ionic conductivity measurements were completed using a Solartron 1260 impedance spectrometer over the frequency range 1 Hz–1 MHz with an amplitude of 100 mV. Arrhenius measurements used a Maccor Environmental chamber over the range 25 °C ≤ T ≤ 100 °C. The samples were formed into pellets of diameter 1.27 cm and were pressed with Al/C blocking electrodes at 300 MPa in a pressurized cell for all electrochemical measurements.
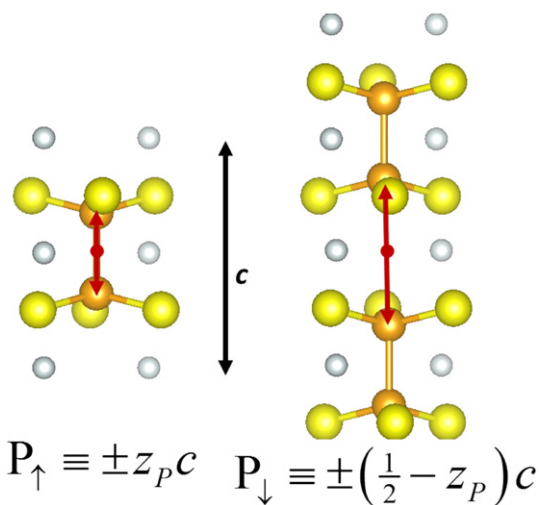

Fig. 2. Ball-and-stick diagram of the P_2S_6 ion units comprising the $Li_4P_2S_6$ crystals. The ball designations are Li, P, S in increasing size with gray, orange, and yellow colors respectively. The red arrows indicate the two possible placements of the P sites within a unit cell centered at the red dot.

2.2. Simulation formalisms and algorithms

The calculational methods used in this work are the same as that used in previous studies of similar materials [13]. Specifically, the calculations are based on density functional theory [14,15], using the projector augmented wave (PAW) [16] formalism. The PAW basis and projector functions were generated by the *ATOMPAW* [17] code and used in both the *ABINIT* [18] and *QUANTUM ESPRESSO* [19] packages. The exchange-correlation functional was the local density approximation (LDA) [20], which has been shown to give excellent results for similar materials provided that a systematic 2% underestimate of the lattice size is taken into account for each of the 3 dimensions. The simulated results reported here (including the simulations of the diffraction patterns) have all been adjusted by multiplying the calculated lengths by 1.02. The calculated fractional coordinates and total energies are assumed to be correct.

The electronic structure calculations were performed with plane wave expansions of the wavefunctions including $|\mathbf{k}+\mathbf{G}|^2 \leq 64$ bohr^{-2} and with a Brillouin zone sampling grid density of at least 0.003 bohr^{-3}. Structural parameters of the model systems were determined by minimizing the calculated total energies. The electronic structure results could be qualitatively analyzed in terms of partial densities of states $N^a(E)$, calculated from the expression

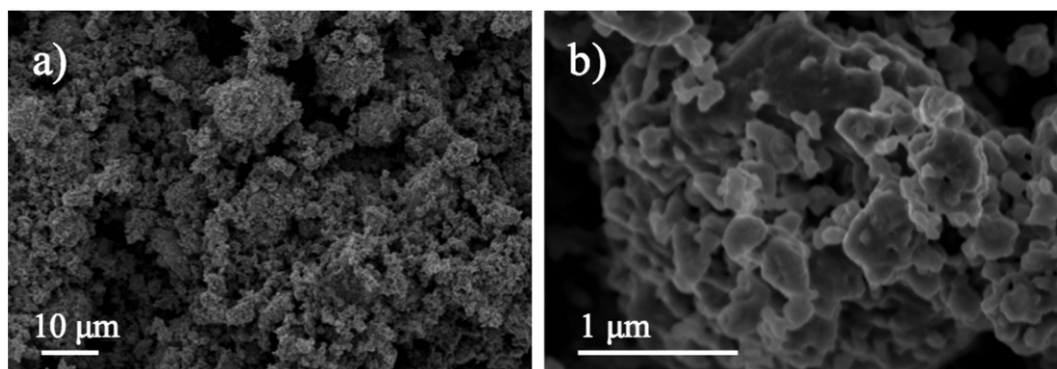$$N^a(E) = \sum_{n\mathbf{k}} W_\mathbf{k} Q_{n\mathbf{k}}^a \delta(E - E_{n\mathbf{k}}), \qquad (2)$$

Fig. 1. Scanning electron microscopy (SEM) images of $Li_4P_2S_6$ (a) after ball milling, and (b) a close-up of the ball milled material showing nanosized particles.
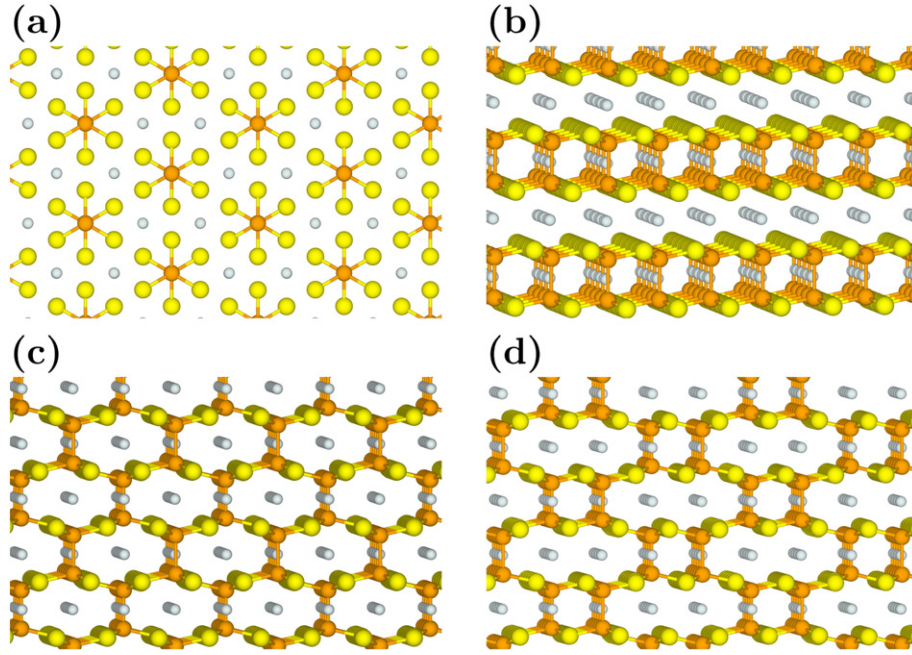
Fig. 3. Ball-and-stick models of $Li_4P_2S_6$ with gray, orange, and yellow balls representing Li, P, and S sites, respectively. Part (a) shows a projection onto the hexagonal plane common to all of the structures. Parts (b)–(d) show a view point with perpendicular and parallel components of the hexagonal plane. Part (b) shows the ordered $P\bar{3}1m$ structure with an energy/formula unit of 0.03 eV higher than the ground state. Part (c) shows an ordered ground state configuration having two formula units per unit cell and $Pnnm$ symmetry. Part (d) shows an ordered ground state configuration having four formula units per unit cell and $Pnma$ symmetry.

as described in previous work [13]. Here a denotes an atomic site, $W_{\mathbf{k}}$ denotes the Brillouin zone sampling weight factor for wave vector $\mathbf{k}$, and $E_{n\mathbf{k}}$ denotes the band energy for band index n and wave vector $\mathbf{k}$. In practice, the δ function is represented by a Gaussian smoothing function with a width of 0.14 eV. For each eigenstate $n\mathbf{k}$ and atomic site a, the local density of states factor $Q_{n\mathbf{k}}^a$ is given by the charge within the augmentation sphere of radius r_c^a which can be well approximated by

$$Q_{n\mathbf{k}}^a \approx \sum_{ij} \left\langle \tilde{\Psi}_{n\mathbf{k}} | p_{n_i l_i m_i}^a \right\rangle \left\langle p_{n_j l_j m_i}^a | \tilde{\Psi}_{n\mathbf{k}} \right\rangle q_{n_i l_i; n_j l_i}^a \delta_{l_i l_j}, \tag{3}$$

in terms of the radial integrals

$$q_{n_i l_i; n_j l_i}^a \equiv \int_0^{r_c^a} dr\, \varphi_{n_i l_i}^a(r) \varphi_{n_j l_j}^a(r). \tag{4}$$

In these expressions, $|\tilde{\Psi}_{n\mathbf{k}}\rangle$ represents a pseudo-wavefunction, $|\tilde{p}_{n_i l_i m_i}^a\rangle$ represents a PAW atomic projector function localized within the augmentation sphere about atomic site a and characterized with radial and spherical harmonic indices $n_i l_i m_i$ [16,21]. The function $\varphi_{n_i l_i}^a(r)$ represents the corresponding all-electron radial basis function. The augmentation radii used in this work are $r_c^{Li} = 1.6$, $r_c^O = 1.2$, $r_c^P = 1.7$, and $r_c^S = 1.7$ in bohr units. The reported partial densities of states, $\langle N^a(E) \rangle$, are averaged over sites of each type a.

The "nudged elastic band" (NEB) method [22–24], as programmed in the *QUANTUM ESPRESSO* package was used to estimate the Li^+ migration energies E_m in supercell models. For this analysis it was assumed that 5 images between each meta-stable configuration was sufficient to estimate the path energies. For these simulations, supercells consisting of 8 formula units were used. The simulations were performed on neutral supercells, either by using a compensating uniform charge, or by modeling an interstitial ion in the presence of a distant vacancy (or visa versa) within the supercell. The migration energies determined from the NEB calculations can be related to the experimental

conductivity σ measurements as a function of temperature T through the Arrhenius relationship[4]

$$\sigma = \sigma_0 e^{-E_A/kT}, \tag{5}$$

where k denotes the Boltzmann constant, E_A represents the activation energy for Li ion migration, and σ_0 denotes a temperature independent constant for the sample. For nearly perfect crystals, thermal processes must initiate the formation of a vacancy and interstitial pair with energy E_f so that $E_A = E_m + \frac{1}{2}E_f$. For crystals with a significant population of native defects, we expect $E_A = E_m$.

Visualizations were constructed using the *XCrySDEN* [26,27] and *VESTA* [28] software packages. The software program *FINDSYM* [29] was used to help analyze the symmetry properties of the optimized structures. In order to directly compare the model structures with the diffraction measurements, powder patterns were generated from the calculated structural parameters using the program Mercury [30] for the X-ray patterns and using the program GSAS [12] for the neutron patterns. The optimized fractional coordinates were used directly, while, as mentioned above, all of the calculated lattice parameters were scaled by a uniform factor of 1.02 in order correct for the systematic size error of the local density approximation (LDA) exchange correlation functional. The diffraction results of Mercier et al. [9] reported here were also generated using the Mercury and GSAS programs.

3. Results

3.1. Crystal properties

$Li_4P_2S_6$ was found to form at increased temperatures between 750 °C and 900 °C in vacuum. The yield of each synthesis process described in

---

[4] This form of the Arrhenius relation lacks the $1/T$ prefactor which comes from the Einstein relation between diffusion and ionic conductivity, such as derived in Ref. [25]. However, this form empirically fits the data well.

Section 2.1.1 was 99%. The purified reaction product included particles having diameters ≥10 μm which were reduced to nanosize after ball-milling. SEM images of the sample after the ball-milling process at two different magnifications are shown in Fig. 1a and b. Producing the nanosized powder aided in pressing dense pellets for electrochemical characterization. This method resulted in pellets as dense as 96% of the ideal density of 2.23 g/cm^3.

3.2. Structural properties

As noted in 1982 by Mercier et al. [9], the building blocks of $Li_4P_2S_6$ crystals are P_2S_6 (hexathiohypodiphosphate) ions having D_{3d} symmetry, oriented with the P–P bond along the crystallographic c axis, as shown in Fig. 2. The left diagram of the figure shows one possible placement of a P_2S_6 ion with the origin of the unit cell at the center of the P–P bond and the coordinates of the P sites designated as $P_\uparrow \equiv \pm z_P c$. The right diagram of the figure shows the other possible placement of the building blocks with the origin of the unit cell located between P_2S_6 units and the coordinates of the P sites designated as $P_\downarrow \equiv \pm (\frac{1}{2} - z_P)c$.

Mercier et al. [9] described the overall structure of $Li_4P_2S_6$ in terms of the space group $P6_3/mcm$ (# 193) [31]. In this designation, using the site multiplicity and Wyckoff symbols, the 4e P sites at fractional coordinates $(0, 0, z_P)$, and three other symmetry equivalent sites, have 0.5 occupancy. On the other hand, the 4d Li sites at fractional coordinates $(1/3, 2/3, 0)$, and three other symmetry equivalent sites, and the 6g S sites at fractional coordinates $(x_S, 0, 1/4)$, and five other symmetry equivalent sites, are fully occupied.

The basic structure of the crystal as projected within a hexagonal plane is shown in Fig. 3a. This structure is common to all of the possible structural variations. The placement of any given P–P bond within a crystal unit determines the placement of all of the P–P bonds along the same c axis. It is reasonable to assume, as is consistent with the experimental analysis, that the S and Li sites are insensitive to these bond placements. The likely structural variations in $Li_4P_2S_6$ crystals can be enumerated on a two-dimensional hexagonal lattice in terms of the $P_\uparrow$ or $P_\downarrow$ placements of P–P bonds on each c axis. Our previous simulation studies [10] found a meta-stable structure which corresponds to choosing all of P–P bonds of the $P_\uparrow$ type which results in a structure with group symmetry of $P\bar{3}1m$ (# 162) [31], which is a subgroup of the Mercier structure. This structure of ordered P–P bonds has an energy of 0.03 eV/formula unit higher than the lowest energy structure, and is shown in Fig. 3b. Other possible structures have P–P bonds in between alternate S layers. For example, the ordered structures shown in Fig. 3c and d are based on orthorhombic supercells of the hexagonal structure having an equal number of $P_\uparrow$ and $P_\downarrow$ sites. These are two examples of

structures computed to have the lowest energy of the configurations considered. The configuration of Struc. (c) has two formula units per unit cell and the crystallographic space group is $Pnnm$ (# 58) [31]. The configuration of Struc. (d) has four formula units per unit cell and the crystallographic space group is $Pnma$ (# 62) [31]. In addition to Struc. (c) and Struc. (d), we have examined several other configurations, generally finding that those configurations with equal numbers of $P_\uparrow$ and $P_\downarrow$ sites have energies equal to that of the ground state, while configurations with unequal numbers of $P_\uparrow$ and $P_\downarrow$ sites have energies between that of the ground state and 0.03 eV which characterizes the pure $P_\uparrow$ setting. While we have by no means explored the vast configuration space of this system, we can reasonably conclude that this system has many configurations corresponding to the ground state and many configurations with energies close to that of the ground state.

In addition to the structural optimization, the computer simulations determine the electronic structure of the materials, the qualitative features of which are exhibited by the partial densities of states. We find the partial densities of states of $Li_4P_2S_6$ to be insensitive to the detailed structures shown in Fig. 3. Fig. 4 shows the partial densities of states for Struc. (d) shown in Fig. 3d and is very similar to the result for the $P\bar{3}1m$ structure [10]. The partial densities of states show that the P–P dimers result in valence band contributions at 1.5 eV lower energy and generally increase the overall valence band width compared to that of γ-Li_3PS_4.

X-ray analysis of the powdered sample was carried out at room temperature and at several lower temperatures and the results are shown in Fig. 5. We expected $P_\uparrow$ and $P_\downarrow$ variations in the structures to result in a temperature dependence of the X-ray data. However, the fact that the 4 patterns are essentially identical indicates no structural transformation in the temperature range 15 K ≤ T ≤ 298 K. This result is somewhat surprising given that calculations have identified many configurations of the P–P bonds resulting in energies in the range of $0 \le E \le 0.03$ eV/formula units relative to the ground state. On the other hand, one expects that there may be significant energy barriers to changing P–P bond configurations, involving either migrations of P_2S_6 units or sequences of breaking and reforming P–P bonds. This reasoning leads to the suggestion that the P–P bond configurations might be "frozen" in at the time that the crystal is formed. The room temperature pattern in this work is essentially identical to the results reported by Mercier et al. [9].

Fig. 6 compares simulated X-ray diffraction patterns for each of the structural variations shown in Fig. 3 with the measured pattern at 15 K. In order to easily compare with the neutron data, the scattering angle Θ has been converted to the normal distance between diffracting planes d according to the Bragg condition $d = \lambda/(2 \sin \Theta)$, where the X-ray wavelength is $\lambda = 1.54056$ Å. The simulated patterns for the ordered supercell structures of Fig. 3 reproduce the main diffraction peaks
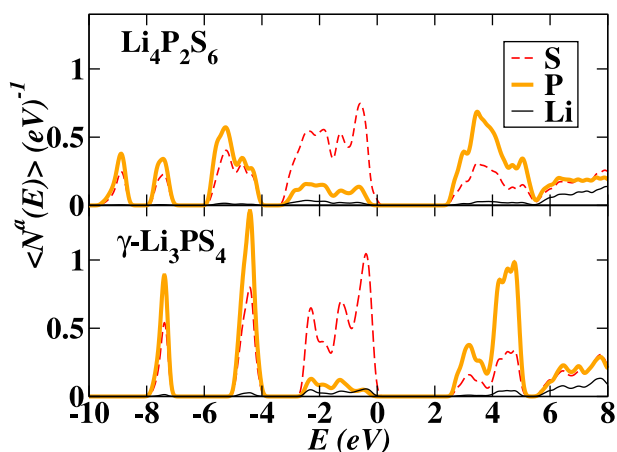

Fig. 4. Partial density of states evaluated using Eq. (2) for $Li_4P_2S_6$ compared with that of γ-Li_3PS_4. The zero of energy is taken as the highest occupied state of the systems.
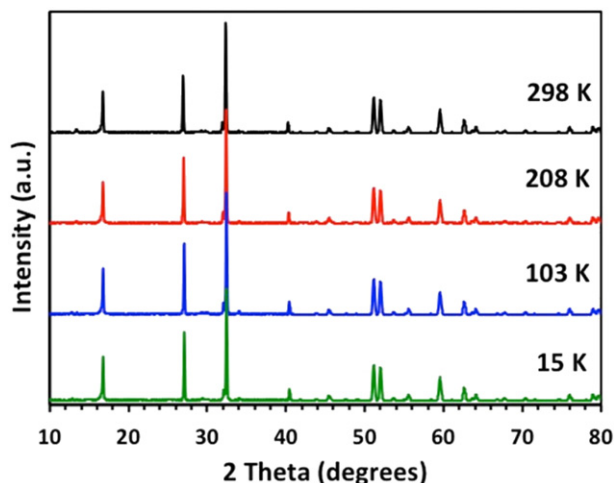

Fig. 5. X-ray powder patterns of $Li_4P_2S_6$ measured at indicated temperatures.
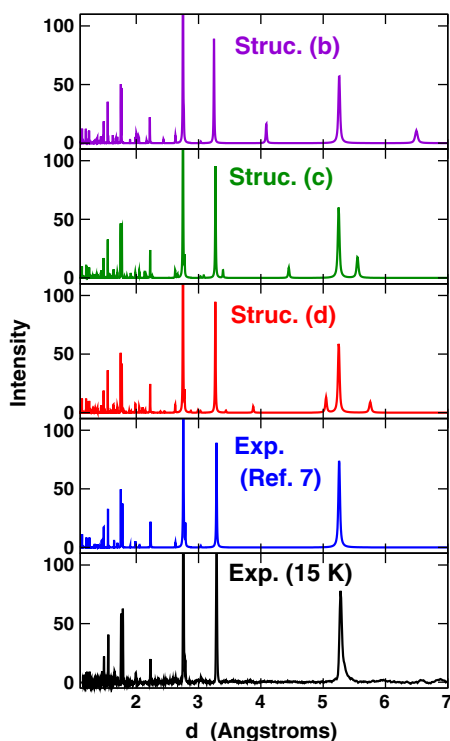
Fig. 6. Simulated X-ray patterns from the structural models shown in Fig. 3, compared with our low temperature X-ray data and the room temperature X-ray data reported by Mercier et al. [9]. The intensity of the data and simulations were normalized so that the highest peaks at approximately $d = 2.75$ Å are fixed at the intensity of approximately 200.
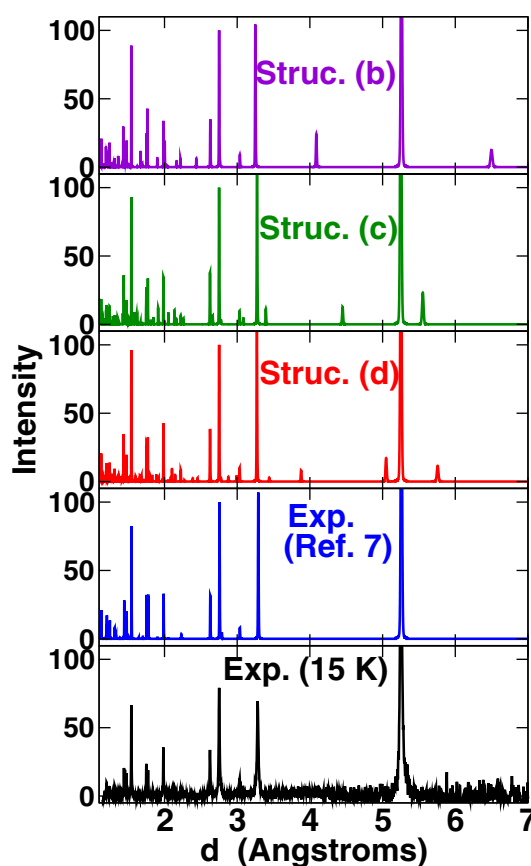

Fig. 7. Simulated neutron diffraction patterns from the structural models shown in Fig. 3, compared with our low temperature neutron data and the room temperature structure by Mercier et al. [9]. The intensity of the data and simulations were normalized so that the highest peaks at approximately $d = 5.25$ Å are fixed at the intensity of approximately 200.

quite well, but differ from the experimental patterns and from each other with the appearance of additional small intensity diffraction peaks mostly apparent at large d. If we assume that the powder sample is composed of grains or domains of material each having one of the possible structures, the diffraction pattern should be composed of an incoherent superposition of diffraction patterns for each of the structures. It is apparent that the incoherent average of the simulated patterns will reduce the intensity of the extra peaks and preserve the main features of the experimental pattern. The Mercier crystal parameters [9] which describe the structure in terms of the 50% occupancy of the P sites generates the same powder diffraction pattern. However, rather than having a completely random occupation, as described in Fig. 2, the actual P site occupation is restricted to $P_\uparrow$ and $P_\downarrow$ configurations.

We can make a similar comparison with the neutron diffraction data shown in Fig. 7. As expected, the diffraction peak positions as a function of diffraction plane distances d are identical in the X-ray and neutron results, but because of the different cross section relationships, the intensity profiles of Figs. 7 and 6 are quite different. The simulated patterns for Struct. (b), (c), and (d) again show extra peaks at large values of d. In the X-ray pattern, the largest diffraction peak occurs at $d = 2.76$ Å which corresponds to 12 equivalent $(2\bar{1}1)$ reflections in the hexagonal unit cell while another strong diffraction peak occurs at $d = 3.29$ Å corresponding to 2 equivalent (002) reflections. In the neutron pattern the largest diffraction peak occurs at $d = 5.26$ Å corresponding to 6 equivalent (100) reflections in the hexagonal unit cell. Interestingly, in these figures, the peak for the largest d value occurs at $d = 6.50$ Å corresponding to a (001) reflection in Struc. (b). For all the other structures and the experimental results, the c-axis symmetry allows only multiples of (002) reflections.

The refinement of our X-ray and neutron data and simulations for the lattice parameters a and c and fractional coordinate parameters z_P and x_S are summarized in Table 1 in terms of the hexagonal $P6_3/mcm$ unit cell. The numerical results are consistent with the conclusions

from analysis of the X-ray patterns of Fig. 5, namely that the structure is invariant with temperature.

3.3. Stability of $Li_4P_2S_6$

The $Li_4P_2S_6$ crystal was found to be thermally stable in vacuum up to 950 °C. Fig. 8 compares the thermal gravimetric analysis (TGA) in Ar and in air. In an atmosphere of Ar gas, there is a small amount of weight loss in the sample, presumably due to a small amount of impurities in the Ar source. By contrast, when placed in air, the sample is stable (losing a weight percent of 2% or less) up to 280 °C. At temperatures higher than 280 °C, $Li_4P_2S_6$ loses nearly 25% of its mass (Fig. 8). Looking at these results in more detail, X-ray diffraction data were taken on the high temperature products at 280 °C and at 350 °C (Fig. 9). In the latter case, reaction products of P_2O_5, $Li_4P_2O_7$, and Li_2SO_4 were identified from the X-ray data. The room temperature pattern of $Li_4P_2S_6$ differs slightly from that shown in Fig. 6 because of small structural changes due to air exposure. Overall, the results indicate that $Li_4P_2S_6$ is much more stable than other lithium thiophosphates. For example Li_3PS_4 decomposes at room temperature in air.

3.4. Electrochemical measurements and simulations

The samples in the form of pressed pellets prepared at 300 MPa have a density of 2.14 g/cm^3. The ball-milled material allowed for the fabrication of denser pellets, which improved the ionic conductivity of $Li_4P_2S_6$. The pellets were pressed with Al/C blocking electrodes to perform all impedance and Arrhenius measurements. The impedance measurements are given in the Appendix A and the corresponding Arrhenius plot of

Table 1
Summary of structural parameters for $Li_4P_2S_6$. Calculated results were averaged from supercell simulations and the lattice parameters were scaled by 1.02 in order to account for the systematic underestimation of lattice size by the LDA exchange-correlation functional.

	a (Å)	c (Å)	z_P	x_S
This work at 15 K (X-ray)	6.051	6.548	0.172	0.324
This work at 15 K (neutron)	6.055	6.553	0.172	0.326
This work at 300 K (X-ray)	6.075	6.597	0.172	0.324
This work at 300 K (neutron)	6.075	6.595	0.173	0.326
Ref. [9]; X-ray at 293 K	6.070	6.577	0.1715	0.3237
Calculated structure b	6.07	6.50	0.18	0.33
Calculated structure c	6.06	6.54	0.17	0.33
Calculated structure d	6.06	6.54	0.17	0.33

Fig. 9. X-ray patterns of $Li_4P_2S_6$ processed at indicated temperatures in air. The $Li_4P_2S_6$ powder was heated/cooled at 100 °C/h to the indicated temperature and held at the temperature for 1 h prior to the X-ray diffraction analysis.

the conductivity derived from the impedance measurements is shown in Fig. 10. The ionic conductivity of $Li_4P_2S_6$ is 2.38×10^{-7} S cm^{-1} at 25 °C and 2.33×10^{-6} S cm^{-1} at 100 °C. These results show that $Li_4P_2S_6$ has an activation energy (as defined by Eq. (5)) of 0.29 eV. This activation energy is smaller than that measured for nano-porous β-Li_3PS_4 ($E_m \approx 0.35$ eV) [5] but larger than the meta-stable superionic conducting material $Li_7P_3S_{11}$ ($E_m \approx 0.12 - 0.18$ eV) [32,33,7].

In order to better understand the mechanism for ion conduction, we have carried out NEB calculations. First, we considered vacancy models based on 8 formula unit supercells of Struc. (d) shown in Fig. 3d. For this structure, unique Li vacancy hops can occur within the hexagonal plane between sites A, B, C, and D and perpendicular to the hexagonal plane between sites C, E, and F as shown in Fig. 11. The corresponding energy versus configuration diagrams are shown in Fig. 12, indicating that the vacancy migration energies are given by $E_m = 0.6$ eV for paths both within a hexagonal plane and perpendicular to the plane. Using a supercell with a similar dimension, we also investigated the migration of vacancies in the $P\bar{3}1m$ structure shown in Fig. 3b, finding a minimum migration energy of $E_m = 0.5$ eV for Li vacancies in a hexagonal layer between P_2S_6 groups. The similarity of these two results suggest that for the vacancy mechanism, the effects of $P_\uparrow$ and $P_\downarrow$ disorder has little effect on Li ion migration barriers. However, by comparison of the calculated migration energies with the experimentally measured activation for $Li_4P_2S_6$, one can conclude that the Li ion conduction is unlikely to be explained by the vacancy hopping mechanism.

We also considered possible interstitial Li ion migration mechanisms, focusing on the 8 formula unit supercells of Struc. (d) shown in Fig. 3d. In order to find possible meta-stable interstitial configurations, we relaxed a sizable number of initial configurations based on a coarse grid of possible interstitial sites with one fixed remote vacancy in
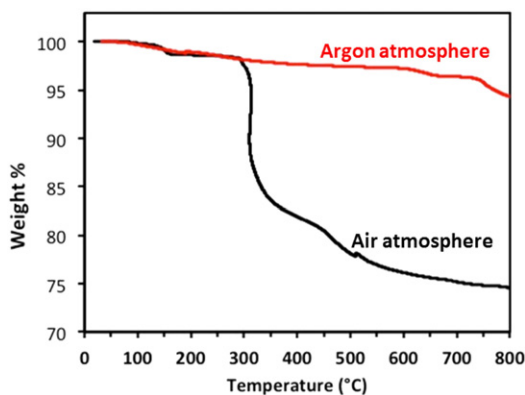

Fig. 10. Arrhenius plot of the ionic conductivity (Eq. (5)) for $Li_4P_2S_6$.

order to keep the simulation cells with zero net charge. Several metastable interstitial sites were found, including the 4 neighboring sites shown in Fig. 13a. While these sites, which are roughly 2 Å apart from each other and from nearby host lattice Li sites, do not span the supercell, they can give a reasonable approximation to a configuration diagram for a pure interstitial mechanism of Li ion migration as shown in Fig. 13b. For this partial path, the migration energy is $E_m = 0.1$ eV, suggesting that it is likely that the interstitial Li ion migration is energetically favorable for this material. More complicated processes, such as an interstitialcy mechanism involving both interstitial and host lattice

Fig. 8. Thermal gravimetric analysis (TGA) of $Li_4P_2S_6$ showing the percentage weight remaining in the sample as a function of temperature when processed in Ar gas (red curve) or in air (black curve). $Li_4P_2S_6$ shows limited thermal stability in air until 280 °C.

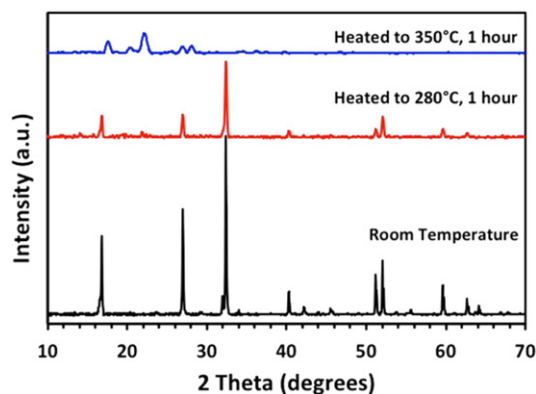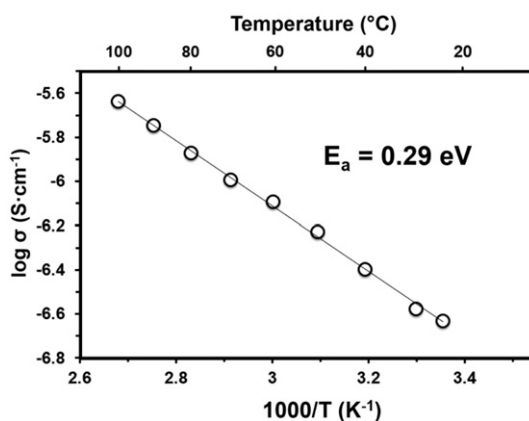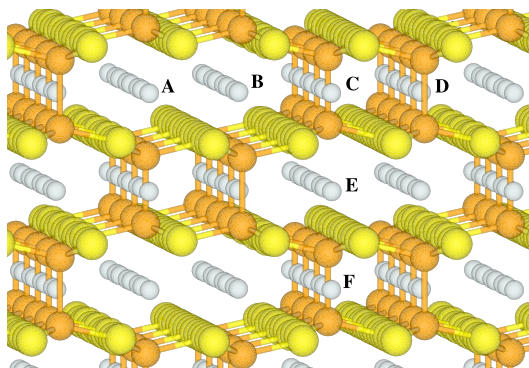**Fig. 11.** Ball-and-stick diagram of supercell of $Li_4P_2S_6$ in Struc. (d) shown in Fig. 3d, indicating vacancy positions A–F. The view point of this diagram is similar to that of Fig. 3d.
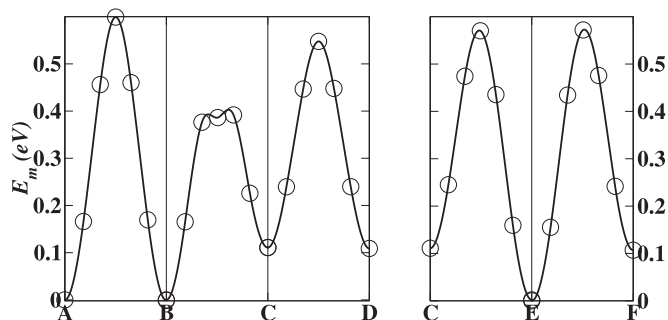
Fig. 12. Energy path diagrams corresponding to the supercell model shown in Fig. 11 determined by NEB calculations of unique vacancy hops within the hexagonal plane (left graph) or along a c axis (right graph). The zero of energy was taken as the lowest vacancy configuration.

Li ions, could also be important for this system. As discussed in Section 2.2, the Arrhenius activation energy E_A can also depend on the "formation" energy to produce an interstitial/vacancy pair, unless the sample has a native population of defects. Our simulations of possible interstitial/vacancy configurations result in an estimate of the formation energy to be more than 1 eV. Therefore, we conclude that our samples must have native populations of defects such Li^+ Frenkel interstitial/vacancy pairs [34].

While we have shown that $Li_4P_2S_6$ is one of the more stable thiophosphate materials as shown in Fig. 8 it is interesting to ask the question of whether it is stable in the presence of a Li anode. When $Li_4P_2S_6$ is exposed to lithium metal, a noticeable reaction occurs between the solid electrolyte and the metal. While our experimental attempts to cycle a $Li/Li_4P_2S_6/Li$ cell have not yet been successful, ideal interfaces of the electrolyte with a Li anode give insight into the system.
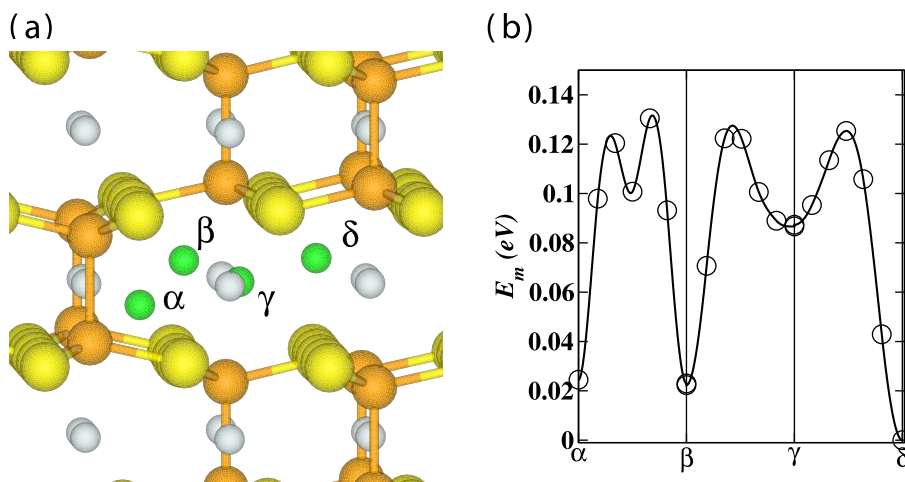

Fig. 13. (a) Ball-and-stick diagram of metastable interstitial sites of the structure shown in Fig. 3d labeled α, β, γ, and δ indicated in green and superposed on ideal lattice of Struc. (d). The view point of this diagram is similar to that of Fig. 3d and that of Fig. 11. (b) NEB energy path diagram for interstitial Li ion migration.
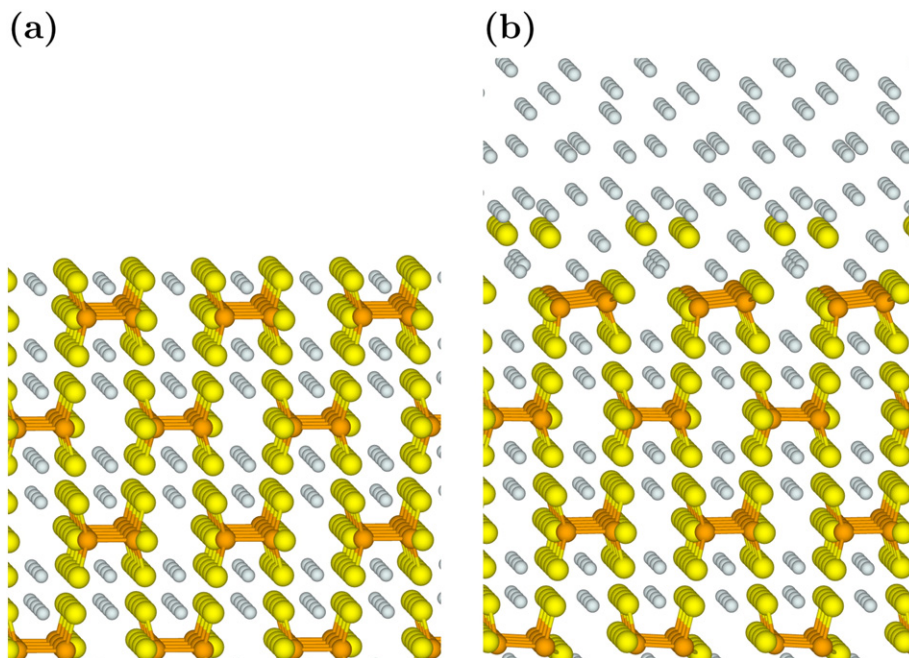

Fig. 14. (a) Relaxed surface structure of $Li_4P_2S_6$ with Struc. (c) (Fig. 3c) cleaved perpendicular to the hexagonal plane with vacuum shown at the top of the diagram. (b) Relaxed structure of the surface in the presence of several layers of Li metal shown at the top of the diagram.
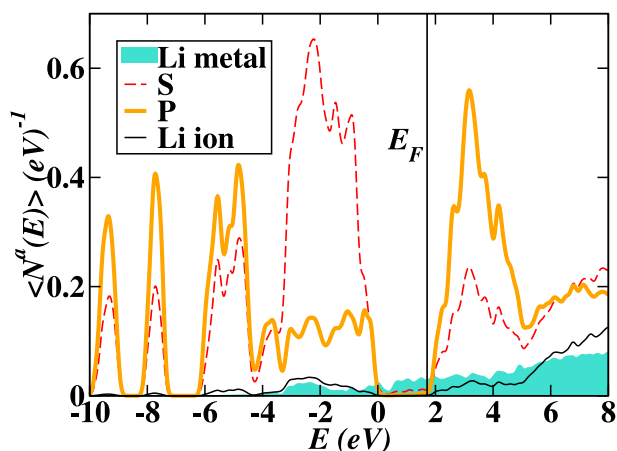
Fig. 15. Partial density of states plot for the idealized interface shown in Fig. 14b. The zero of energy is adjusted to the bulk partial density of states plot of $Li_4P_2S_6$.
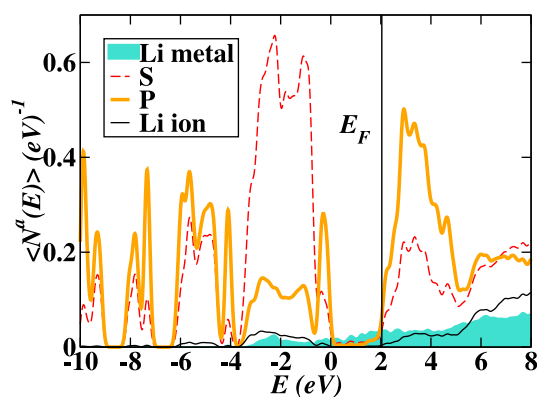

Fig. 17. Partial density of states plot for the idealized interface shown in Fig. 16b. The zero of energy is adjusted to the bulk partial density of states plot of $Li_4P_2S_6$.

For example, we considered one idealized cleavage of the crystal in a plane containing the hexagonal axis and containing complete P_2S_6 units as shown in Fig. 14a. When this surface is exposed to an idealized Li metal interface and the system was allowed to relax, the system showed some decomposition as shown in Fig. 14b. In this case, S–P bonds in the outer layer break in a similar way to that observed in the Li_3PS_4/Li system [13]. For $Li_4P_2S_6$/Li there seems to be a buffer layer of Li_2S formed at the interface, while the P–P bonds remained intact. The partial density of states plot for this system is shown in Fig. 15.

Another example cleave was taken parallel to the hexagonal plane. In order to maintain the P_2S_6 building blocks, this cleave results in a rough surface as shown in Fig. 16a. When Li metal layers are introduced into this supercell, the relaxed structure has broken P–S bonds and Li_2S groups form. The optimized geometry is very sensitive to the details of the initial structure, an example of which is shown in Fig. 16b. In most of the cases studied the P–P bonds remained intact. The partial density of states is shown in Fig. 17.

4. Summary and conclusions

We have prepared and investigated pure samples of $Li_4P_2S_6$. In particular, we have shown that the disorder in the structure

first identified by Mercier et al. [9] is due to energetic degeneracy in the placement of the P_2S_6 building blocks of the structure. The simulation results are consistent with the X-ray and neutron diffraction measurements. We rationalize the observation that the structure is invariant with temperature by noting that within a given structure, transformation between the possible P–P bond placements must have a high energy barrier. The relative stability of $Li_4P_2S_6$ compared with Li_3PS_4 correlates with its increased valence band width.

The activation energy determined from the Arrhenius conductivity measurements is $E_A = 0.29$ eV, which is quite favorable. However for the samples we prepared, the magnitude of the ionic conductivity is very low. Simulations indicate that the mechanism for ionic conduction in this material is likely to involve interstitial processes. If the concentration of interstitial Li ions could be increased, perhaps the ionic conductivity could be improved. The impedance measurements were made using blocking electrodes. Cells prepared with pure Li electrodes could only be cycled a few times before shorting. Simulations on ideal surfaces suggest that the $Li_4P_2S_6$/Li interface can form a meta-stable buffer layer as does Li_3PS_4 [13]. However, experiments show that for $Li_4P_2S_6$/Li, this meta-stability is very fragile and typically not realized, in contrast to the Li_3PS_4/Li system [5].

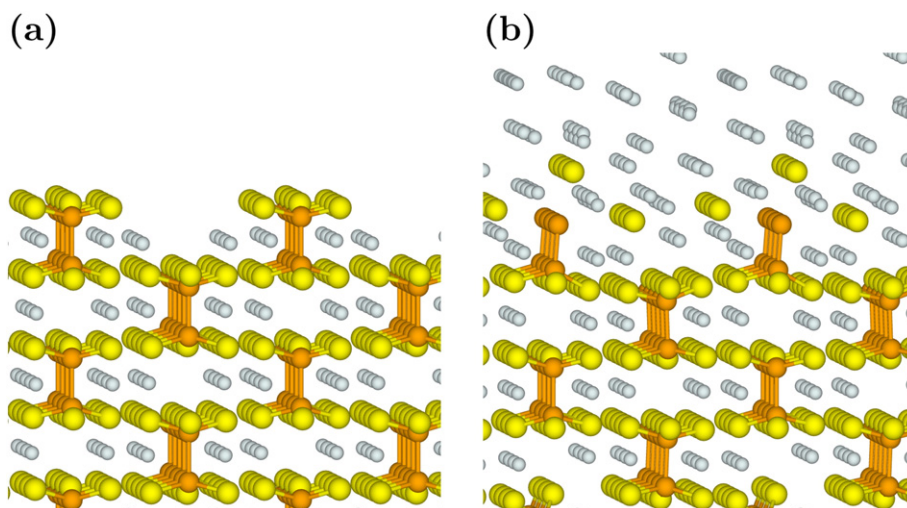**Fig. 16.** (a) Relaxed surface structure of $Li_4P_2S_6$ in Struc. (c) (Fig. 3c) cleaved parallel to the hexagonal plane with vacuum shown at the top of the diagram. (b) Relaxed structure of the surface in the presence of several layers of Li metal shown at the top of the diagram.

The current study has enhanced our understanding of the Li thiophosphate family of solid electrolytes, finding that $Li_4P_2S_6$ is formed at temperatures of 750 °C or higher and shows prolonged stability in air when compared to other lithium thiophosphates. The results of this study provide insights towards better understanding of the family of lithium thiophosphate solid electrolytes as one of the very promising candidate materials for the implementation of safe high energy-dense batteries for large scale energy storage.

More generally, there are other members of the family of materials based on P_2S_6 (hexathiohypodiphosphate) building blocks as recently shown by Kuhn et al. [35], including $Na_4P_2S_6$, which may provide interesting comparisons to the present work and may be of interest to battery technology.

Acknowledgments

Appendix A

A Nyquist or Cole–Cole plot of the real and imaginary parts of the impedance curves for $Li_4P_2S_6$ is shown in Fig. 18. The total ionic conductivity reported in Fig. 10 and detailed in Table 2 is determined by using the intercept of the semi-circle and the straight line as the resistance.
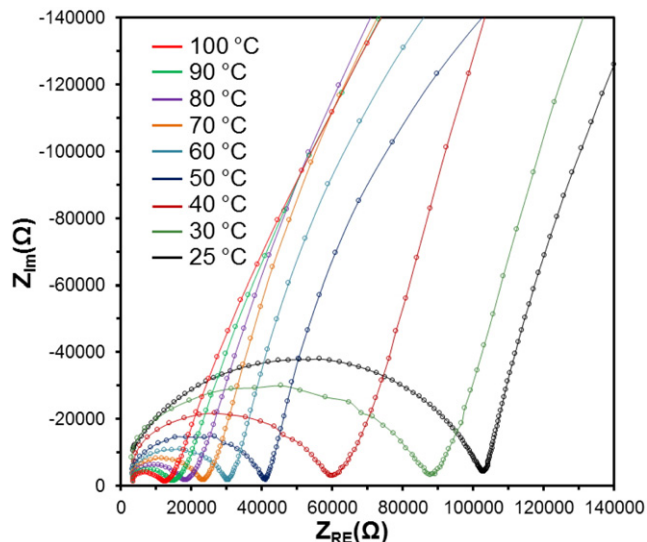

Fig. 18. Impedance measurements for $Li_4P_2S_6$ at temperatures between 25 °C and 100 °C using blocking electrodes attached to the pellet having cross sectional area 1.27 cm^2 and thickness 0.03 cm. These impedance measurements are representative of results from other $Li_4P_2S_6$ pellets of similar size.

Table 2
Resistances and calculated ionic conductivities of $Li_4P_2S_6$ at different temperatures.

Temperature (°C)	R (Ω)	σ (S/cm)
25	101,030	2.38×10^{-7}
30	88,975	2.70×10^{-7}
40	59,143	4.06×10^{-7}
50	40,017	6.00×10^{-7}
60	29,326	8.18×10^{-7}
70	23,216	1.03×10^{-6}
80	17,537	1.37×10^{-6}
90	13,856	1.82×10^{-6}
100	10,283	2.33×10^{-6}

References

[1] Arthur L. Robinson, Jügen Janek, MRS Bull. 39 (2014) 1046–1047.
[2] Juchuan Li, Cheng Ma, Miaofang Chi, Chengdu Liang, Nancy J. Dudney, Adv. Energy Mater. 5 (2015) 1401408.
[3] Yan Wang, William Davison Richards, Shyue Ping Ong, Lincoln J. Miara, Jae Chul Kim, Yifei Mo, Gerbrand Ceder, Nat. Mater. 14 (2015) 1026–1031 (URL http://www.nature.com/doifinder/10.1038/nmat4369).
[4] Noriaki Kamaya, Kenji Homma, Yuichiro Yamakawa, Masaaki Hirayama, Ryoji Kanno, Masao Yonemura, Takashi Kamiyama, Yuki Kato, Shigenori Hama, Koji Kawamoto, Akio Mitsui, Nat. Mater. 100 (9) (2011) 682–686.
[5] Zengcai Liu, Wujun Fu, E. Andrew Payzant, Xiang Yu, Zili Wu, Nancy J. Dudney, Jim Kiggans, Kunlun Hong, Adam J. Rondinone, Chengdu Liang, J. Am. Chem. Soc. 1350 (3) (2013) 975–978.
[6] Keiichi Minami, Akitoshi Hayashi, Masahiro Tatsumisago, J. Ceram. Soc. Jpn. 118 (2010) 305–308.
[7] Akitoshi Hayashi, Keiichi Minami, Masahiro Tatsumisago, J. Solid State Electrochem. 14 (2010) 1761–1767.
[8] Independent private communication from Ezhiylmurugan Rangasamy and Zachary Hood 2013.
[9] R. Mercier, J.P. Malugani, B. Fahys, J. Douglade, G. Robert, J. Solid State Chem. 43 (1982) 151–162.
[10] N.A.W. Holzwarth, N.D. Lepley, Yaojun A. Du, J. Power Sources 196 (2011) 6870–6876.
[11] Keiichi Minami, Fuminori Mizuno, Akitoshi Hayashi, Masahiro Tatsumisago, Solid State Ionics 178 (2007) 837–841.
[12] A.C. Larson, R.B. Von Dreele, Los Alamos National Laboratory Report LAUR 86-748-748, 2004.
[13] N.D. Lepley, N.A.W. Holzwarth, Yaojun A. Du, Phys. Rev. B 88 (2013) 104103.
[14] P. Hohenberg, W. Kohn, Phys. Rev. 136 (1964) B864–B871.
[15] W. Kohn, L.J. Sham, Phys. Rev. 140 (1965) A1133–A1138.
[16] P.E. Blöchl, Phys. Rev. B 50 (1994) 17953–17979.
[17] N.A.W. Holzwarth, A.R. Tackett, G.E. Matthews, Comput. Phys. Commun. 135 (2001) 329–347 (Available from the website http://pwpaw.wfu.edu).
[18] X. Gonze, B. Amadon, P.M. Anglade, J.M. Beuken, F. Bottin, P. Boulanger, F. Bruneval, D. Caliste, R. Caracas, M. Cote, T. Deutsch, L. Genovese, Ph. Ghosez, M. Giantomassi, S. Goedecker, D.R. Hamann, P. Hermet, F. Jollet, G. Jomard, S. Leroux, M. Mancini, S. Mazevet, M.J.T. Oliveira, G. Onida, Y. Pouillon, T. Rangel, G.M. Rignanese, D. Sangalli, R. Shaltaf, M. Torrent, M.J. Verstraete, G. Zerah, J.W. Zwanziger, Comput. Phys. Commun. 180 (12) (2009) 2582–2615 (Code is available at the website http://www.abinit.org).
[19] Paolo Giannozzi, Stefano Baroni, Nicola Bonini, Matteo Calandra, Roberto Car, Carlo Cavazzoni, Davide Ceresoli, Guido L. Chiarotti, Matteo Cococcioni, Ismaila Dabo, Andrea Dal Corso, Stefano de Gironcoli, Stefano Fabris, Guido Fratesi, Ralph Gebauer, Uwe Gerstmann, Christos Gougoussis, Anton Kokalj, Michele Lazzeri, Layla Martin-Samos, Nicola Marzari, Francesco Mauri, Riccardo Mazzarello, Stefano Paolini, Alfredo Pasquarello, Lorenzo Paulatto, Carlo Sbraccia, Sandro Scandolo, Gabriele Sclauzero, Ari P. Seitsonen, Alexander Smogunov, Paolo Umari, Renata M. Wentzcovitch, J. Phys. Condens. Matter 21 (39) (2009) 394402 (Available from the website http://www.quantum-espresso.org).
[20] John P. Perdew, Yue Wang, Phys. Rev. B 45 (1992) 13244–13249.
[21] N.A.W. Holzwarth, G.E. Matthews, R.B. Dunning, A.R. Tackett, Y. Zeng, Phys. Rev. B 55 (1997) 2005–2017.
[22] H. Jónsson, G. Mills, K.W. Jacobsen, in: B.J. Berne, G. Ciccotti, D.F. Coker (Eds.), Classical and Quantum Dynamics in Condensed Phase Simulations, World Scientific, Singapore 1998, pp. 385–404.
[23] Graeme Henkelman, Blas P. Uberuaga, Hannes Jónsson, J. Chem. Phys. 113 (2000) 9901–9904.
[24] Graeme Henkelman, Hannes Jónsson, J. Chem. Phys. 113 (2000) 9978–9985.
[25] Ryogo Kubo, J. Phys. Soc. Jpn. 12 (1957) 570–586.
[26] Anton Kokalj, J. Mol. Graph. Model. 17 (1999) 176–179 (Code available at the website http://www.xcrysden.org).
[27] Anton Kokalj, Comput. Mater. Sci. 28 (2003) 155–168.
[28] Koichi Momma, Fujio Izumi, Appl. Crystallogr. 44 (2011) 1272–1276 (Code available from the website http://jp-minerals.org/vesta/en/).
[29] H.T. Stokes, D.M. Hatch, J. Appl. Crystallogr. 38 (2008) 237–238 (Available from the webpage http://iso.byu.edu/iso/isotropy.php).
[30] Mercury 3.5.1, Developed and Distributed by the Cambridge Crystallographic Data Centre, http://www.ccdc.cam.ac.uk/mercury/2014.

[31] Th. Hahn (Ed.), International Tables for Crystallography, Volume A: Space-group Symmetry, Fifth revised editionKluwer, ISBN: 0-7923-6590-9, 2002.

[32] Fuminori Mizuno, Akitoshi Hayashi, Kiyoharu Tadanaga, Masahiro Tatsumisago, Solid State Ionics 177 (2006) 2721–2725.

[33] Masahiro Tatsumisago, Akitoshi Hayashi, J. Non-Cryst. Solids 354 (2008) 1411–1417.

[34] W. Hayes, A.M. Stoneham, Defects and Defect Processes in Nonmetallic Solids, John Wiley & Sons, 1985.

[35] Alexander Kuhn, Roland Eger, Jürgen Nuss, Bettina V. Lotsch, Z. Anorg. Allg. Chem. 640 (5) (2014) 689–692.